PHYSICAL REVIEW A **112**, 052814 (2025)

Postselection effect in the spectroscopy of the helium $2\,^3S - 2\,^3P$ transition

Jia-Dong Tang (唐家栋),[1,*] Jin-Lu Wen (温金录),[2,*] Jun-Feng Dong (董俊峰),[3]
Yu R. Sun (孙羽),[2,†] Ya-Nan Lv (吕亚男),[1] and Shui-Ming Hu (胡水明)[1,3]
[1]*Hefei National Research Center for Physical Sciences at the Microscale,*
University of Science and Technology of China, Hefei 230026, China
[2]*Institute of Advanced Light Source Facilities, Shenzhen 518107, China*
[3]*Hefei National Laboratory, University of Science and Technology of China, Hefei 230088, China*

(Received 11 June 2025; accepted 9 October 2025; published 17 November 2025)

We present a theoretical and experimental investigation of the postselection effect in precision spectroscopy of the $2\,^3S - 2\,^3P$ transition in helium using an atomic beam. By employing the Monte Carlo wave function (MCWF) method, we simulate the time evolution of the ground and excited amplitudes in the presence of laser fields, revealing a systematic dependence of the measured transition frequency on the spatial parameters of the detection slit, including its position and width. Our results demonstrate that postselection—an inherent aspect of quantum projection in such measurements—can induce frequency shifts on the order of tens of kilohertz. By elucidating the underlying physical mechanisms, our study offers a practical framework for quantitatively correcting the postselection-induced shifts, thereby improving the accuracy of atomic beam spectroscopy.

DOI: 10.1103/n47z-tg2d

I. INTRODUCTION

Precision spectroscopy of few-electron atomic systems provides a powerful tool for testing fundamental physics. Due to their relatively simple energy-level structure, these systems allow for rigorous *ab initio* calculations based on quantum electrodynamics (QED) as well as accurate determination of fundamental physical constants. By comparing high-precision spectroscopic measurements with theoretical predictions, stringent tests of QED can be performed, while discrepancies may hint at novel physical phenomena. A notable example is the "proton radius puzzle," which emerged when the nuclear charge radius extracted from muonic hydrogen spectroscopy disagreed with that derived from electronic hydrogen measurements [1–3]. This discrepancy has spurred extensive experimental and theoretical investigations in both electronic and muonic systems [4–9]. While recent studies have achieved consistency in the isotope shifts of hydrogen and deuterium, the extracted nuclear charge radii in isolated measurements remain unresolved [10,11]. A similar discrepancy exists in helium spectroscopy. Measurements of the $2\,^3S - 2\,^3P$ transition in ^{4}He have yielded two kilohertz-precision results differing by approximately 50 kHz [12–15]. This inconsistency suggests the presence of unaccounted systematic errors in these experiments. Recent efforts in both electronic and muonic helium systems have sought to clarify these discrepancies [16–25], yet a complete resolution remains elusive.

In our recent work, we identified a systematic effect of postselection (PS) that considerably impacts precision spectroscopy in atomic beam experiments [19]. This effect arises when a slit selects atoms based on their transverse momentum, inadvertently modifying the observed transition frequency. The PS-induced shift, which can reach tens of kilohertz—far exceeding typical experimental uncertainties—has likely influenced past measurements without being properly accounted for. Postselection is conceptually related to weak measurement amplification in quantum optics, where selective detection introduces shifts in observed quantities [26,27]. In atomic beam spectroscopy, the Doppler effect is a dominant systematic error, often mitigated by transverse collimation using slits. However, this collimation inherently selects atoms with specific momentum states, leading to a frequency shift if the selection correlates with the measured observable. Since this effect is subtle and difficult to detect experimentally, a thorough theoretical and numerical analysis is essential for accurate corrections.

In this work, we present a detailed investigation of the postselection effect in precision helium spectroscopy. Using the Monte Carlo wave function (MCWF) method, we simulate atomic evolution and momentum changes under various experimental conditions, including slit geometry, atomic beam properties, and laser configurations (standing and traveling waves). Our simulations quantitatively reproduce the observed shifts and provide a framework for correcting systematic biases. Applying this analysis to previous measurements [14], we derive a correction of about 55 kHz, bringing the result into agreement with our postselection-free measurement [19]. Our work establishes a general methodology for identifying and correcting postselection effects in precision spectroscopy, with broad implications for high-precision measurements of nuclear charge radii and other fundamental quantities.

II. EXPERIMENTAL

The experimental setup used to investigate the postselection effect is illustrated in Fig. 1. A laser-cooled atomic beam

---

[*] These authors contributed equally to this work.

[†] Contact author: sunyu@mail.iasf.ac.cn

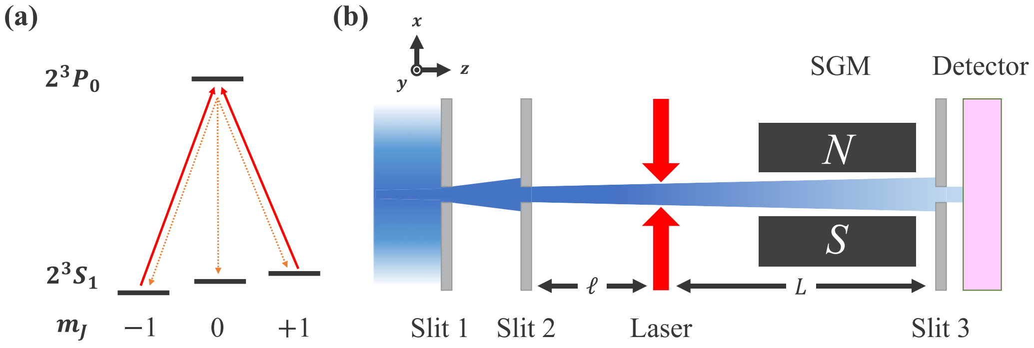

FIG. 1. (a) Energy diagram of the $2\,^3P_0 - 2\,^3S_1$ transition in a magnetic field. (b) Experimental setup. The collimated helium atomic beam is prepared in the 2^3S_1, $m = \pm 1$ states before entering the slit region. Atoms are deflected by a Stern-Glarch magnet if there is no probe laser. Some atoms would be excited by the probe laser and undergo spontaneous decay to the $m = 0$ state with a certain probability, which could pass through the narrow slit and get detected by the multichannel plate detector. A spectrum is acquired by recording the atomic signal as the laser frequency is scanned. The probe laser is scanned around the resonance of the $2\,^3S_1 - 2\,^3P_0$ transition, which is divided into two counterpropagating laser beams. Traveling-wave and standing-wave measurements could be achieved by periodically blocking the two lasers.

of metastable helium in the 2^3S_1 state propagates along the z axis and passes sequentially through three slits, labeled as Slit 1, Slit 2, and Slit 3, while the detector is located immediately downstream of Slit 3. Slit 2 and Slit 3 are translatable along the x axis and can be fully retracted if needed. Prior to entering the slit region, the atoms are optically pumped into either the $m = +1$ or -1 Zeeman sublevels, depending on the polarization of the pumping laser. In the absence of resonant interaction with the probing laser, atoms remain in their initial magnetic substate and are deflected by a Stern-Gerlach magnet (SGM), producing no detectable signal. However, when the probing laser frequency is tuned near the $2\,^3S_1 - 2\,^3P_0$ transition, some atoms are excited and subsequently decay via spontaneous emission, with a probability of populating the $m = 0$ state. These atoms, unaffected by the SGM, can traverse Slit 3 and reach the detector. By scanning the probing laser frequency and recording the atomic signal, a spectrum is acquired. The transition frequency is then determined by fitting the spectrum to a Lorentzian profile.

A feedback servo was employed to dynamically maintain the probing laser perpendicular to the atomic beam. The spectrum can be recorded under either standing-wave or traveling-wave configurations using the SCTOP (sequential counterpropagating traveling-wave optical pulses) method [28]. For standing-wave measurements, the probing beam is retroreflected, and a single spectrum is recorded. For traveling-wave measurements, two spectra are recorded separately using the upper and lower probing beams (see Fig. 1). More details on the experimental setup and detection methodology can be found in Ref. [28].

III. MONTE CARLO WAVE FUNCTION METHOD

To systematically investigate postselection effects, we employed the MCWF method for atomic trajectory simulations. This approach is particularly suited to address the inherent complexity of simultaneously modeling quantum transitions and the evolution of atomic momentum and position in beam experiments. The MCWF method provides an efficient framework for studying small quantum systems coupled to dissipative environments [29], where fluctuations and dissipation manifest through stochastic quantum jumps during time evolution. This approach applies to Markovian systems with Lindblad-type relaxation operators and is formally equivalent to the standard master equation formalism [30]. For systems with large Hilbert spaces, the wave function method offers computational advantages over density matrix approaches, as it requires tracking only N components compared to N^2 elements in the density matrix. The MCWF method thus enables efficient simulation of atomic beam experiments.

The computational complexity of MCWF scales as $\mathcal{O}(N)$, significantly lower than the $\mathcal{O}(N^2)$ scaling of master equation methods, making it particularly suitable for simulating light-atom interactions in complex systems [15,31–37].

We consider an atomic system comprising an excited state $|e\rangle$, a ground state $|g\rangle$, and a metastable dark state. Ground-state atoms may absorb photons to reach $|e\rangle$, while excited atoms can either radiatively decay back to $|g\rangle$ or transition to the dark state. The quantum interference effect [38] for the studied transition is estimated to be around 0.06(2) kHz [19]. Since this is negligible compared to the experimental uncertainty, we disregard its contribution in our analysis. We defined the atomic beam direction as the z axis and the probe propagation along the x axis. Since previous experiments were performed in both traveling-wave and standing-wave configurations [14,28], we conducted theoretical simulations for both field geometries using the MCWF method. While the general derivation of the MCWF approach is provided in the Appendix, we focus here only on the aspects relevant to the present study.

A. Traveling-wave field

In the traveling-wave field configuration, for a unidirectional probe light propagating along the $+x$ axis with zero initial phase, the field can be expressed as

$$E(x, t) = E_0 \cos(\omega t - kx). \tag{1}$$

The effective Hamiltonian can then be expressed as

$$H_{\mathrm{eff}} = \frac{P^2}{2M} + \frac{\hbar\Omega}{2}(e^{ikx}S^+ + e^{-ikx}S^-) - \hbar\Delta P_e - \frac{i\hbar}{2}\Gamma P_e, \tag{2}$$

where Δ is frequency detuning, $P_e = |e\rangle\langle e|$ is the projection operator, $S^+ = |e\rangle\langle g|$, $S^- = |g\rangle\langle e|$, and Ω is the Rabi frequency.

For the system under study, we adopt the basis $\{|e, p\rangle, |g, p\rangle\}$, where p represents the momentum. The momentum space is discretized with a step size of $\hbar k$, where k is the wave vector of the light. Consequently, the normalized wave function can be expressed as

$$|\Psi(t)\rangle = \sum_n c_{e,n}(t)\,|e, n\hbar k\rangle + c_{g,n}(t)\,|g, n\hbar k\rangle. \tag{3}$$

Here, the coefficients $c_{e,n}(t)$ and $c_{g,n}(t)$ represent the probability amplitudes at time t for the atom to be in the excited state $|e\rangle$ and ground state $|g\rangle$, respectively, with a momentum projection of $n\hbar k$ along the x axis.

For the $2\,^3S_1 - 2\,^3P_0$ transition under study, we set the probe laser frequency to resonate with the $2\,^3S_1(m = +1) - 2\,^3P_0(m = 0)$ transition, where the $2\,^3S_1(m = +1)$ and $2\,^3P_0(m = 0)$ states are defined as $|g\rangle$ and $|e\rangle$, respectively. The dark states include the $2\,^3S_1(m = 0)$ and $2\,^3S_1(m = -1)$ states. Atoms in the excited state spontaneously decay to $|g\rangle$, $m = 0$ dark state, or $m = -1$ dark state, each with an equal probability of 1/3.

Initially, due to optical pumping, the atomic population predominantly resides in $|g\rangle$ and the $m = -1$ dark state. After passing through the slits and interacting with the probe light, only atoms ultimately in the $m = 0$ dark state contribute to the detection signal due to Stern-Gerlach magnet filtering.

Let v_z be the longitudinal velocity along the atomic beam direction and v_0 the initial transverse velocity along the x axis. In our experiment, the spread in longitudinal velocity v_z is maintained below 5 m/s [39]. Our previous work [19] showed that a 5-m/s variation in v_z induces a subkilohertz-level change in the postselection effects, demonstrating the insensitivity of these effects to longitudinal velocity distribution. We therefore approximate v_z by its mean value, neglecting its spread. For the transverse motion, we consider only the x component v_x, given by

$$v_x = v_0 + \frac{n\hbar k}{M}. \tag{4}$$

If no quantum jump occurs within a sufficiently small time interval δt, the wave function evolves to $|\Psi^{(1)}(t + \delta t)\rangle$ at time $t + \delta t$, given by

$$|\Psi^{(1)}(t + \delta t)\rangle = \left(1 - \frac{iH_{\text{eff}}\delta t}{\hbar}\right)|\Psi(t)\rangle\,. \tag{5}$$

Substituting Eqs. (2)–(4) into Eq. (5), we obtain the time evolution of the system's wave function amplitude, which takes the form

$$\begin{aligned} c^{(1)}_{e,n}(t + \delta t) = c_{e,n}(t) - i\frac{\delta t}{\hbar}\Bigg\{\Bigg[\frac{(n\hbar k + Mv_0)^2}{2M} \\ - \hbar\Delta - \frac{i\hbar\Gamma}{2}\Bigg]c_{e,n}(t) + \frac{\hbar\Omega}{2}c_{g,n-1}(t)\Bigg\}, \end{aligned} \tag{6}$$

$$\begin{aligned} c^{(1)}_{g,n}(t + \delta t) = c_{g,n}(t) - i\frac{\delta t}{\hbar}\Bigg\{\frac{(n\hbar k + Mv_0)^2}{2M}c_{g,n}(t) \\ + \frac{\hbar\Omega}{2}c_{e,n+1}(t)\Bigg\}. \end{aligned} \tag{7}$$

B. Standing-wave field

In the standing-wave configuration, we perform the derivation using a similar approach. For the standing-wave field formed by counterpropagating probe beams along the x axis with zero initial phase, we have

$$\begin{aligned} E &= E_0\cos(\omega t - kx) + E_0\cos(\omega t + kx) \\ &= E_0\cos(kx)(e^{i\omega t} + e^{-i\omega t}). \end{aligned} \tag{8}$$

The effective Hamiltonian can then be expressed as

$$H_{\text{eff}} = \frac{P^2}{2M} + \frac{\hbar\Omega}{2}(e^{ikx} + e^{-ikx})(S^+ + S^-) - \hbar\Delta P_e - \frac{i\hbar}{2}\Gamma P_e. \tag{9}$$

Following a derivation procedure analogous to the traveling-wave case, we obtain the time evolution of the wave function amplitudes for the standing-wave system, which takes the form

$$\begin{aligned} c^{(1)}_{e,n}(t + \delta t) = c_{e,n}(t) - i\frac{\delta t}{\hbar}\Bigg\{\Bigg[\frac{(n\hbar k + Mv_0)^2}{2M} - \hbar\Delta \\ - \frac{i\hbar\Gamma}{2}\Bigg]c_{e,n}(t) + \frac{\hbar\Omega}{2}[c_{g,n+1}(t) + c_{g,n-1}(t)]\Bigg\}, \end{aligned} \tag{10}$$

$$\begin{aligned} c^{(1)}_{g,n}(t + \delta t) = c_{g,n}(t) - i\frac{\delta t}{\hbar}\Bigg\{\Bigg[\frac{(n\hbar k + Mv_0)^2}{2M} - \hbar\Delta \\ - \frac{i\hbar\Gamma}{2}\Bigg]c_{g,n}(t) + \frac{\hbar\Omega}{2}[c_{e,n+1}(t) + c_{e,n-1}(t)]\Bigg\}. \end{aligned} \tag{11}$$

C. Spontaneous emission

During stimulated photon absorption, atoms transition from $|g, n\hbar k\rangle$ to $|e, (n \pm 1)\hbar k\rangle$, where the sign depends on the photon propagation direction ($\pm x$). Conversely, stimulated emission induces transitions from $|e, n\hbar k\rangle$ to $|g, (n \pm 1)\hbar k\rangle$, with the sign determined by the emitted photon's direction. In our simulations, we consider a momentum range of $-10\hbar k$ to $+10\hbar k$, with the wave function comprising $N = 42$ basis states.

For spontaneous emission, we model the recoil momentum projection along x as discrete changes in the atom's transverse velocity. Following spontaneous decay, atoms transition from $|e, n\hbar k\rangle$ to either $|g, n\hbar k\rangle$ or dark states, with their x-direction velocity modified to

$$v_0^{(1)} = v_0 - \frac{\hbar k}{M}\sin\theta\cos\phi, \tag{12}$$

where θ and ϕ denote the spherical angles of the spontaneously emitted photon in three-dimensional (3D) space. We note that atomic spontaneous emission exhibits angular anisotropy [30], with the emission intensity distribution for different polarization transitions following

$$I^{(\sigma^\pm)}(\theta, \varphi) \propto \frac{1 + \cos^2\theta}{2}, \tag{13}$$

$$I^{(\pi)}(\theta, \varphi) \propto \sin^2\theta. \tag{14}$$

The initial transverse velocity is then updated to $v_0 = v_0^{(1)}$.

If the atom decays to the dark state $m = 0$, it no longer interacts with the light. In this case, the wave function probability amplitude of the atom corresponds to the final state after leaving the laser field, which is given by

$$c_{e,n} = 0, \tag{15}$$

$$c_{0,n} = \frac{c_{e,n}^{(1)}(t+\delta t)}{\sum_{m=-\infty}^{+\infty}\left|c_{e,m}^{(1)}(t+\delta t)\right|^2}. \tag{16}$$

Using the longitudinal velocity v_z of the atoms, we can calculate the time intervals before and after the interaction with the probe light. From the transverse velocities before and after the probe interaction, we determine the transverse position of the atom at the slit in front of the detector. Combining this with the corresponding probabilities $|c_{0,n}|^2$, we obtain the probability of the atom passing through the slit and being detected.

IV. RESULTS AND DISCUSSION

A. PS effects with a narrow Slit 3

We investigated the postselection effect under different conditions. Both experiments and simulations were conducted with a beam longitudinal velocity of $v_z = 290$ m/s and a laser power of 1 μW. Some results represent power extrapolations and will be explicitly noted. Unlike the SCTOP method, which fixes the slit position and changes the laser incident direction during the measurement, our approach kept the laser incident direction fixed and as perpendicular as possible to the atomic beam. For comparison, the experimental results are presented as relative values normalized to the final result of the SCTOP method. In simulations, the absence of a postselection effect corresponds to a result of 0 kHz.

We first fixed the positions of Slit 1 and Slit 2, each with a width of 0.3 mm, at the center of the atomic beam along the x direction. Without applying the pump-probe process, we measured the initial beam distribution by translating Slit 3 (width 0.5 mm). The measured distribution had a FWHM of approximately 1.5 mm, corresponding to a divergence angle of about 0.1 mrad. By varying the lateral position of Slit 3, we investigated the influence of the postselection effect on the results. As shown in Fig. 2, the experimental results (red solid circles) agree well with the theoretical simulations (blue hollow diamonds). The uncertainty in the theoretical simulations corresponds to the statistical uncertainty inherent in the MCWF method. Our relative values are referenced to the experimental results obtained by our group using the SCTOP method, as detailed in Ref. [28]. The corresponding results are indicated by the black dashed line in Fig. 2. Conceptually, this method can be viewed as employing an extremely wide Slit 3, and we consider its outcomes to be free from postselection effects. Hence, we adopt these values as the reference frequencies for relative measurements. Notably, the postselection effect at Slit 3 induces a significant frequency shift, which remains consistent across different lateral positions of Slit 3. These findings align with our earlier work [19], where postselection effects were studied via distribution measurements. The observed frequency deviation quantifies the impact of postselection on the experimental results.

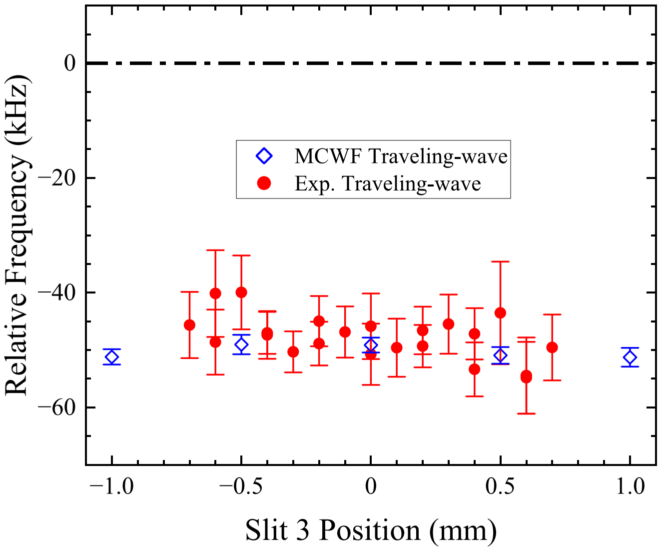

FIG. 2. Postselection shifts at different Slit 3 positions in measurements including Slit 1 and Slit 2, each with a width of 0.3 mm and fixed at the center of the atomic beam. The black dashed line represents the result without the postselection effect. Red solid circles represent experimental results, while the blue hollow diamonds represent the simulation results obtained using the MCWF method.

The postselection effect arises from the momentum selection of atoms by Slit 3. Consequently, varying the slit width alters this selection effect, leading to changes in the induced frequency shift. To verify this, we employed the MCWF method, simulating postselection effects for Slit 3 widths ranging from 0.5 to 6 mm. The results are presented in Fig. 3. In the simulation, Slit 3 was fixed at the transverse center

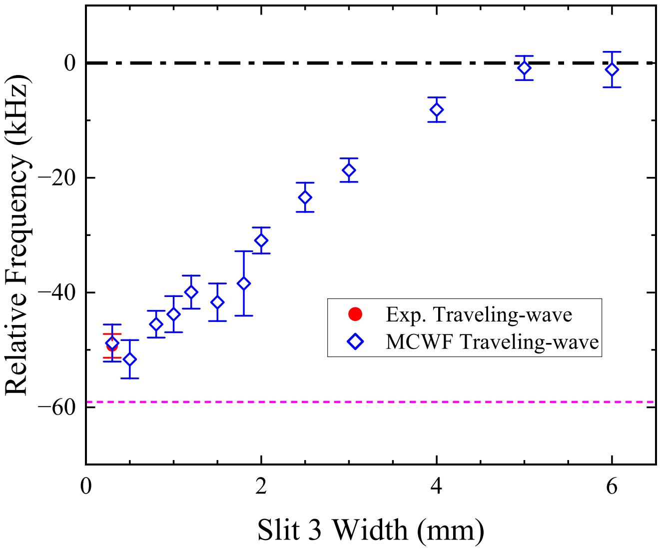

FIG. 3. Postselection shifts at different widths of Slit 3, with the slit center fixed. Each result has been extrapolated to the zero power. The red dot represents the experimental result given in Fig. 2, and the result converges to zero without the postselection effect (or with a very wide Slit 3), shown as the black dashed line. The pink dashed line represents the calculation result of Eq. (17).

position while its width was adjusted. The results reveal that the postselection shift decreases when the width increases. At a very narrow width of Slit 3, the results agree with the phenomenological model presented in our previous work [19]:

$$\frac{f_{\mathrm{PS}}}{f_c} = -\frac{v_R}{c}\frac{L}{\ell + L}, \tag{17}$$

where f_{PS} is the PS shift, f_c is the center frequency of the transition, v_R is the recoil velocity from photon absorption, c is the speed of light, ℓ is the distance from Slit 2 to the probing position, and L is the distance from the probing position to Slit 3. With the Slit 3 width of over 5 mm, the postselection effect vanishes, and the results converge with those obtained without Slit 3. These simulations indicate that in this experiment, a slit width exceeding 5 mm effectively eliminates postselection-induced distortions in the measurements. Due to the limitations of the experimental conditions, only results under 0.3 mm or infinite width conditions could be obtained in the experiment. However, the simulation results of the MCWF method well complement the transition trend of the results between these two extreme conditions.

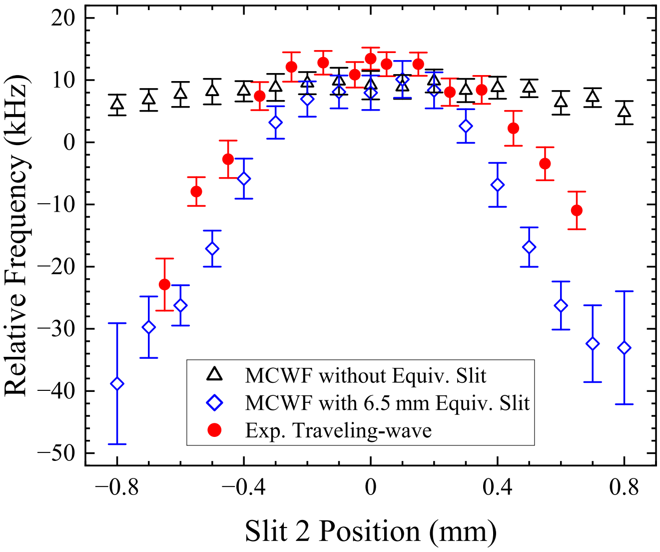

FIG. 4. The measurement and simulation results when Slit 3 is removed, with Slit 1 fixed at the center, and the lateral position of Slit 2 is varied. In the case where the limited width of the Stern-Gerlach magnet is not considered, the MCWF simulation results are represented by the black hollow triangles in the figure. The red solid circles represent the experimental results. When considering an equivalent slit of 6.5-mm width at the exit of the Stern-Gerlach magnet, the MCWF simulation results are shown as blue hollow diamonds in the figure.

B. Spatial constraints and PS effect without Slit 3

Due to experimental factors such as magnetic field gradients, spatial constraints on the millimeter scale (equivalent to a wide slit) may also induce postselection frequency shifts. Since these constraints cannot be probed by moving Slit 3 alone, we removed Slit 3 and instead varied the position of Slit 2 to investigate their effects. With Slit 1 fixed at the beam center, displacing Slit 2 significantly alters the incident atomic beam direction. Any spatial constraints in the setup would then manifest as pronounced frequency shifts during this directional change. As shown in Fig. 4, simulations ignoring spatial constraints (black hollow triangles) predict stable frequencies across all incident directions. However, experimental results (red solid circles) exhibit a bilateral redshift, confirming the presence of postselection effects from spatial limitations. Given that the narrowest section of our setup is the ∼10-mm-diameter SGM pipe (with potential misalignment further restricting the effective beam width), we introduced variable-width slits at the SGM exit in simulations. The best agreement with experimental data (blue hollow diamonds) occurred for a slit width of 6.5 mm.

In principle, two approaches should yield equivalent results: (1) varying the atomic beam's incident direction while keeping the laser angle fixed, and (2) varying the laser's incident angle while maintaining a fixed beam direction. Both methods modify the relative angle between the laser and atomic beam. However, the presence of spatial constraints in our experimental setup breaks this symmetry. When we fix Slits 1 and 2 at the beam center and scan the laser angle, we observe a stable frequency shift. In this configuration, the laser's influence on the beam distribution is minimal, with the atomic trajectories remaining confined within a 6.5 mm width—sufficiently narrow to avoid postselection effects from spatial constraints. This finding is consistent with earlier results (Fig. 3), which showed that postselection becomes negligible for a Slit 3 width exceeding 5 mm. Conversely, when we fix the laser angle and displace Slit 2 laterally, we observe a systematic frequency redshift. This occurs because Slit 2 now acts as a preselection element, filtering atoms with specific transverse velocities. As Slit 2 moves further from the beam center, an increasing fraction of atoms are blocked by the finite aperture of the SGM after interacting with the probe light. This demonstrates how preselection can amplify postselection effects in spatially constrained systems. Our simulations incorporating a 6.5-mm equivalent slit (representing the SGM's effective aperture) confirmed that this constraint has negligible impact when Slit 3 is present. This is because the strong momentum selection of Slit 3 dominates over the weaker spatial selection imposed by the SGM's dimensions. Thus, while spatial constraints become significant when studying the system through Slit 2 displacement, their effect can be safely ignored in configurations where Slit 3 provides the primary selection mechanism.

C. PS effects in standing-wave configurations

While the previous experimental and simulation analysis focused on traveling-wave conditions, we must examine postselection effects under standing-wave configurations to fully characterize our system. With Slit 3 removed and Slit 2 position varied, the standing-wave measurement results (red circles in Fig. 5) reveal a characteristic double-peak pattern. Notably, while significant Slit 2 displacements from center produce redshifted frequencies in both traveling- and standing-wave cases, the key differences emerge near the beam center. The standing-wave measurements exhibit a particularly strong central redshift exceeding 100 kHz. Our simulations, incorporating the finite width of the SGM (green

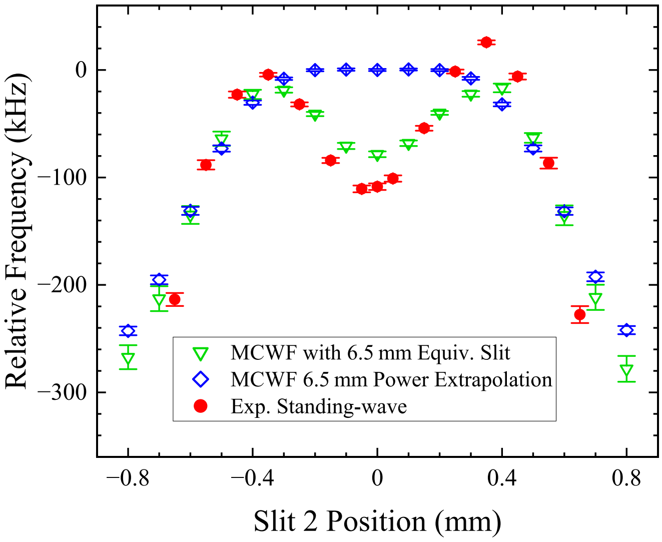

FIG. 5. Frequency shifts corresponding to different lateral positions of Slit 2 in the configuration where Slit 3 was removed and a standing-wave probe laser was applied. Red solid circles represent the experimental results, while green open triangles indicate the frequency shift obtained from MCWF simulations considering the 6.5-mm width of the Stern-Gerlach magnet. The corresponding laser power is 1 μW. Blue open triangles show the simulation results after power extrapolation to the zero-power limit.

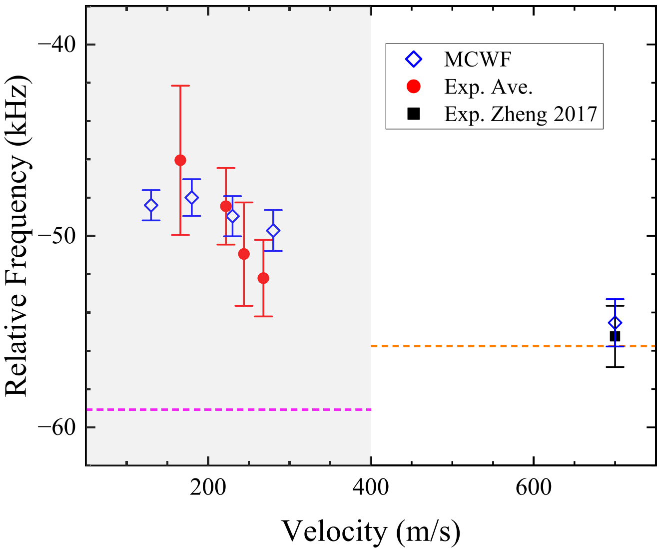

FIG. 6. PS shifts at different beam velocities when only Slits 1 and 3 present in the experiment. Data in the shadow with velocities below 300 m/s show the results under the conditions of the current experimental setup, while the data with a velocity of about 700 m/s present the results from the experiment in Ref. [14]. The red solid circles and black squares represent the experimental results, while the blue open diamonds denote the simulation results using the MCWF method. The pink and orange dashed lines represent the calculation results of Eq. (17) under respective experimental conditions.

hollow triangles in Fig. 5), show excellent agreement with these experimental observations. We attribute the standing- and traveling-wave differences primarily to power-dependent effects, as evidenced by the much steeper power extrapolation slope for standing-wave fields compared to traveling waves [28]. Through simulations at varying power levels followed by extrapolation (blue hollow diamonds in Fig. 5), we observe a pronounced redshift for large Slit 2 displacements. However, when Slit 2 is near the center, the results are almost the same under either traveling-wave or standing-wave fields. This power-corrected analysis confirms that the standing wave's distinctive features are most apparent in off-center configurations, while central measurements converge across both optical field configurations.

In the previous experiment by Zheng *et al.* [14], the setup featured only Slit 1 before the probe light and Slit 3 before the detector (equivalent to the configuration shown in Fig. 1 with just Slits 1 and 3). In this configuration, the single preprobe slit (Slit 1) resulted in a broad initial velocity distribution of the atomic beam. Consequently, the postselection-induced frequency shift showed minimal variation with changes in longitudinal velocity (v_z). This behavior differs significantly from our current dual-slit configuration (Slits 1 and 2), which produces a narrower initial velocity distribution, as we have detailed in our earlier work [19]. Due to the inclusion of a Zeeman decelerator in our current setup, we were unable to reproduce the 700-m/s atomic beam velocity used in the earlier experiment. Instead, we performed measurements at four velocity points using only Slits 1 and 3 (red solid circles in Fig. 6), with corresponding simulations shown as blue open diamonds. Note that simulations assumed a nearly infinitely wide velocity distribution while a finite distribution width after Slit 1 presents in experiments. These distribution differences explain the discrepancies between experimental and simulated results. Furthermore, the current experimental apparatus differs in length from the previous setup. We performed simulations based on the parameters of the previous experiment by Zheng *et al.* [14], which resulted in a postselection frequency shift of −55.3(1.5) kHz, with the error representing the statistical uncertainty of the MCWF calculation. After applying this correction, the result from the previous experiment agreed with our most recent measurements, where postselection effects were eliminated [19].

V. CONCLUSION

This work systematically analyzes the postselection effects induced by slits in the measurement of the helium atom $2\,^3S - 2\,^3P$ transition. Through the combination of high-precision experimental measurements and MCWF simulations that track atomic evolution and momentum changes, we investigated postselection effects under various experimental parameters including slit sizes, slit positions, and different optical field configurations (traveling versus standing waves). Our simulations enabled a precise correction of +55.3(1.5) kHz to the previous experimental result by Zheng *et al.* [14], with the corrected data showing excellent agreement with new measurements performed under postselection-free conditions. The MCWF simulation method developed in this work provides a comprehensive approach for modeling postselection effects by simultaneously accounting for atomic transition processes and the evolution of atomic momentum and position. While this method reduces computational complexity compared to solving full master equations, it remains computationally demanding due to the extensive sparse matrix operations required. For preliminary estimates of postselection effects, the phenomenological approach proposed in our previous work [19] may serve as a practical alternative. For example, in a recent determination of the ionization energy of metastable triplet helium $2\,^3S_1$, the postselection shift had been taken into account and listed in the systematic error budget [40].

Our results demonstrate that postselection effects can induce considerable frequency shifts in precision measurements. This finding strongly suggests that similar systematic deviations may exist in other experiments affected by postselection effects, highlighting the need for further investigation through both simulations and experimental studies. Given the widespread use of slits and small apertures in precision spectroscopy experiments, many such measurements are likely susceptible to postselection effects.

ACKNOWLEDGMENTS

This work was jointly supported by the National Natural Science Foundation of China (Grants No. 12393822, No. 22241301, and No. 12374465) and the Innovation Program for Quantum Science and Technology (Grant No. 2021ZD0303102).

DATA AVAILABILITY

The data that support the findings of this article are openly available [41].

APPENDIX: GENERAL DERIVATION OF MCWF

The Hamiltonian of the atomic system in an optical field can be written as

$$H_s = H_A + V_{A-L} = \frac{\vec{P}^2}{2M} + \hbar\omega_0\,|e\rangle\,\langle e| - \vec{d}\cdot\vec{E}, \tag{A1}$$

where M is the atomic mass, $\vec{P}$ is the atomic momentum, ω_0 is the transition frequency from the ground state to the excited state, $\vec{d}$ is the dipole moment, and $\vec{E}$ is the light field strength.

At time t, the system is described by a normalized wave function $|\Psi(t)\rangle$. If no quantum jump occurs within a sufficiently small time interval δt, the wave function evolves to $|\Psi^{(1)}(t+\delta t)\rangle$ at time $t+\delta t$.The effective Hamiltonian governing the time evolution can be expressed as

$$\begin{aligned} H_{\text{eff}} &= H_s - \frac{i\hbar}{2}\sum_m C_m^\dagger C_m \\ &= \frac{\vec{P}^2}{2M} + \hbar\omega_0\,|e\rangle\,\langle e| - \vec{d}\cdot\vec{E} - \frac{i\hbar}{2}\sum_m C_m^\dagger C_m, \end{aligned} \tag{A2}$$

where C_m is the quantum jump operator, m represents the index of the final state (the ground state or a dark state), and we have

$$\sum_m C_m^\dagger C_m = \Gamma\,|e\rangle\,\langle e|. \tag{A3}$$

At time t, since the wave function is normalized, we have

$$\sum_{n=-\infty}^{+\infty}[|c_{e,n}(t)|^2 + |c_{g,n}(t)|^2] = 1. \tag{A4}$$

After evolving to time $t+\delta t$, the new wave function is no longer normalized. We obtain the probability amplitudes $c_{e,n}^{(1)}(t+\delta t)$ and $c_{g,n}^{(1)}(t+\delta t)$ at time $t+\delta t$, which satisfy the following relations:

$$\Delta P = 1 - \sum_{n=-\infty}^{+\infty}\left[\left|c_{e,n}^{(1)}(t+\delta t)\right|^2 + \left|c_{g,n}^{(1)}(t+\delta t)\right|^2\right], \tag{A5}$$

where ΔP represents the probability of spontaneous emission occurring between time t and $t+\delta t$.

To determine the normalized wave function probability amplitudes at time $t+\delta t$, we evaluate whether spontaneous emission occurs between t and $t+\delta t$. A uniformly distributed random number $\epsilon\in[0,1]$ is generated. If $\epsilon > \Delta P$, spontaneous emission does not occur during this interval, and the normalized wave function probability amplitudes at $t+\delta t$ are given by

$$c_{e,n}(t+\delta t) = \frac{c_{e,n}^{(1)}(t+\delta t)}{\sqrt{1-\Delta P}}, \tag{A6}$$

$$c_{g,n}(t+\delta t) = \frac{c_{g,n}^{(1)}(t+\delta t)}{\sqrt{1-\Delta P}}. \tag{A7}$$

If $\epsilon < \Delta P$, spontaneous emission occurs between t and $t+\delta t$. The atom may decay to the ground state $|g\rangle$, the dark state $m=-1$, or the dark state $m=0$.

If the atom decays to the dark state $m=-1$, it no longer interacts with the light and, due to the Stern-Gerlach magnet, cannot be detected. Therefore, we no longer consider this atom in our analysis.

If the atom decays to the ground state $|g\rangle$, the normalized wave function probability amplitude at time $t+\delta t$ is given by

$$c_{e,n}(t+\delta t) = 0, \tag{A8}$$

$$c_{g,n}(t+\delta t) = \frac{c_{e,n}^{(1)}(t+\delta t)}{\sum_{m=-\infty}^{+\infty}\left|c_{e,m}^{(1)}(t+\delta t)\right|^2}. \tag{A9}$$

After obtaining the normalized wave function probability amplitudes at time $t+\delta t$, we repeat the above procedure until the atom completely exits the laser field, thereby determining the final wave function probability amplitudes after the atom leaves the laser field.

[1] R. Pohl, A. Antognini, F. Nez, F. D. Amaro, F. Biraben, J. M. R. Cardoso, D. S. Covita, A. Dax, S. Dhawan, L. M. P. Fernandes, A. Giesen, T. Graf, T. W. Haensch, P. Indelicato, L. Julien, C.-Y. Kao, P. Knowles, E.-O. L. Bigot, Y.-W. Liu, J. A. M. Lopes *et al.*, Nature (London) **466**, 213 (2010).

[2] A. Antognini, F. Nez, K. Schuhmann, F. D. Amaro, F. Biraben, J. M. Cardoso, D. S. Covita, A. Dax, S. Dhawan, M. Diepold,

L. M. Fernandes, A. Giesen, A. L. Gouvea, T. Graf, T. W. Hansch, P. Indelicato, L. Julien, C. Y. Kao, P. Knowles, F. Kottmann *et al.*, Science **339**, 417 (2013).

[3] P. J. Mohr, B. N. Taylor, and D. B. Newell, Rev. Mod. Phys. **84**, 1527 (2012).

[4] A. Beyer, L. Maisenbacher, A. Matveev, R. Pohl, K. Khabarova, A. Grinin, T. Lamour, D. C. Yost, T. W. Hänsch, N. Kolachevsky, and T. Udem, Science **358**, 79 (2017).

[5] H. Fleurbaey, S. Galtier, S. Thomas, M. Bonnaud, L. Julien, F. Biraben, F. Nez, M. Abgrall, and J. Guéna, Phys. Rev. Lett. **120**, 183001 (2018).

[6] N. Bezginov, T. Valdez, M. Horbatsch, A. Marsman, A. C. Vutha, and E. A. Hessels, Science **365**, 1007 (2019).

[7] W. Xiong, A. Gasparian, H. Gao, D. Dutta, and M. Khandaker, Nature (London) **575**, 147 (2019).

[8] A. Grinin, A. Matveev, D. C. Yost, L. Maisenbacher, V. Wirthl, R. Pohl, T. W. Hänsch, and T. Udem, Science **370**, 1061 (2020).

[9] A. D. Brandt, S. F. Cooper, C. Rasor, Z. Burkley, A. Matveev, and D. C. Yost, Phys. Rev. Lett. **128**, 023001 (2022).

[10] K. Pachucki, V. Lensky, F. Hagelstein, S. S. Li Muli, S. Bacca, and R. Pohl, Rev. Mod. Phys. **96**, 015001 (2024).

[11] P. J. Mohr, D. B. Newell, B. N. Taylor, and E. Tiesinga, Rev. Mod. Phys. **97**, 025002 (2025).

[12] P. C. Pastor, G. Giusfredi, P. D. Natale, G. Hagel, C. de Mauro, and M. Inguscio, Phys. Rev. Lett. **92**, 023001 (2004).

[13] P. C. Pastor, G. Giusfredi, P. D. Natale, G. Hagel, C. de Mauro, and M. Inguscio, Phys. Rev. Lett. **97**, 139903(E) (2006).

[14] X. Zheng, Y. R. Sun, J.-J. Chen, W. Jiang, K. Pachucki, and S.-M. Hu, Phys. Rev. Lett. **119**, 263002 (2017).

[15] X. Zheng, Y. R. Sun, J.-J. Chen, J.-L. Wen, and S.-M. Hu, Phys. Rev. A **99**, 032506 (2019).

[16] D. Shiner, R. Dixson, and P. Zhao, Phys. Rev. Lett. **72**, 1802 (1994).

[17] D. Shiner, R. Dixson, and V. Vedantham, Phys. Rev. Lett. **74**, 3553 (1995).

[18] P. Cancio Pastor, L. Consolino, G. Giusfredi, P. De Natale, M. Inguscio, V. A. Yerokhin, and K. Pachucki, Phys. Rev. Lett. **108**, 143001 (2012).

[19] J.-L. Wen, J.-D. Tang, Y.-N. Lv, Y. R. Sun, C.-L. Zou, J.-F. Dong, and S.-M. Hu, Sci. Adv. **11**, eadu9796 (2025).

[20] R. van Rooij, J. S. Borbely, J. Simonet, M. D. Hoogerland, K. S. E. Eikema, R. A. Rozendaal, and W. Vassen, Science **333**, 196 (2011).

[21] R. J. Rengelink, Y. van der Werf, R. P. M. J. W. Notermans, R. Jannin, K. S. E. Eikema, M. D. Hoogerland, and W. Vassen, Nat. Phys. **14**, 1132 (2018).

[22] Y. van der Werf, K. Steinebach, R. Jannin, H. L. Bethlem, and K. S. E. Eikema, Science **388**, 850 (2025).

[23] J. J. Krauth, K. Schuhmann, M. A. Ahmed, F. D. Amaro, P. Amaro, F. Biraben, T.-L. Chen, D. S. Covita, A. J. Dax, M. Diepold, L. M. P. Fernandes, B. Franke, S. Galtier, A. L. Gouvea, J. Götzfried, T. Graf, T. W. Hänsch, J. Hartmann, M. Hildebrandt, P. Indelicato *et al.*, Nature (London) **589**, 527 (2021).

[24] K. Schuhmann, L. M. P. Fernandes, F. Nez, M. A. Ahmed, F. D. Amaro, P. Amaro, F. Biraben, T.-L. Chen, D. S. Covita, A. J. Dax, M. Diepold, B. Franke, S. Galtier, A. L. Gouvea, J. Götzfried, T. Graf, T. W. Hänsch, M. Hildebrandt, P. Indelicato, L. Julien *et al.*, Science **388**, 854 (2025).

[25] G. Clausen and F. Merkt, Phys. Rev. Lett. **134**, 223001 (2025).

[26] Y. Aharonov, D. Z. Albert, and L. Vaidman, Phys. Rev. Lett. **60**, 1351 (1988).

[27] J. Dressel, M. Malik, F. M. Miatto, A. N. Jordan, and R. W. Boyd, Rev. Mod. Phys. **86**, 307 (2014).

[28] J.-L. Wen, J.-D. Tang, J.-F. Dong, X.-J. Du, S.-M. Hu, and Y. R. Sun, Phys. Rev. A **107**, 042811 (2023).

[29] J. Dalibard, Y. Castin, and K. Mølmer, Phys. Rev. Lett. **68**, 580 (1992).

[30] K. Mølmer, Y. Castin, and J. Dalibard, J. Opt. Soc. Am. B **10**, 524 (1993).

[31] A. Imamog¯lu and L. You, Phys. Rev. A **50**, 2642 (1994).

[32] Y. Castin and K. Mølmer, Phys. Rev. Lett. **74**, 3772 (1995).

[33] F. Intravaia, S. Maniscalco, J. Piilo, and A. Messina, Phys. Lett. A **308**, 6 (2003).

[34] S. Ohta, M. Nakano, R. Kishi, H. Takahashi, and S. Furukawa, Chem. Phys. Lett. **419**, 70 (2006).

[35] F. Sievers, N. Kretzschmar, D. R. Fernandes, D. Suchet, M. Rabinovic, S. Wu, C. V. Parker, L. Khaykovich, C. Salomon, and F. Chevy, Phys. Rev. A **91**, 023426 (2015).

[36] M. Schemmer, A. Johnson, R. Photopoulos, and I. Bouchoule, Phys. Rev. A **95**, 043641 (2017).

[37] V. I. Romanenko and L. P. Yatsenko, Phys. Rev. A **103**, 043104 (2021).

[38] A. Marsman, M. Horbatsch, and E. A. Hessels, Phys. Rev. A **86**, 040501(R) (2012).

[39] J.-J. Chen, Y. R. Sun, J.-L. Wen, and S.-M. Hu, Phys. Rev. A **101**, 053824 (2020).

[40] G. Clausen, K. Gamlin, J. A. Agner, H. Schmutz, and F. Merkt, Phys. Rev. A **111**, 012817 (2025).

[41] J.-D. Tang, Postselection effect in the spectroscopy of the helium $2^3S - 2^3P$ transition, Mendeley Data, V1 (2025), doi: 10.17632/jkdvjxtx68.1.